Standing wave-induced tidal shear in a submarine canyon in the Rockall

² Trough

3	Yuchen Ma ^{1,*}				
4	Raffaele Ferrari ¹				
5	Kurt Polzin ²				
6	Matthew H. Alford ³				
7	Alberto C. Naveira Garabato ⁴				
8	Gunnar Voet ³				
9	¹ Massachusetts Institute of Technology				
10	² Woods Hole Oceanographic Institution				
11	³ Scripps Institution of Oceanography				
12	⁴ University of Southampton				

 * Corresponding author: Yuchen Ma, yuchenma@mit.edu

Preprint status

13

- This manuscript is a non–peer-reviewed preprint submitted to EarthArXiv.
- 16 It has been submitted for peer review to Journal of Physical Oceanography.

Standing wave-induced tidal shear in a submarine canyon in the Rockall

Trough

23

24

Yuchen Ma,^a Raffaele Ferrari,^a Kurt Polzin,^b Matthew H. Alford, ^c Alberto C. Naveira
Garabato, ^d Gunnar Voet, ^c

^a Massachusetts Institute of Technology,

^b Woods Hole Oceanographic Institution,

^c Scripps Institution of Oceanography,

^d University of Southampton

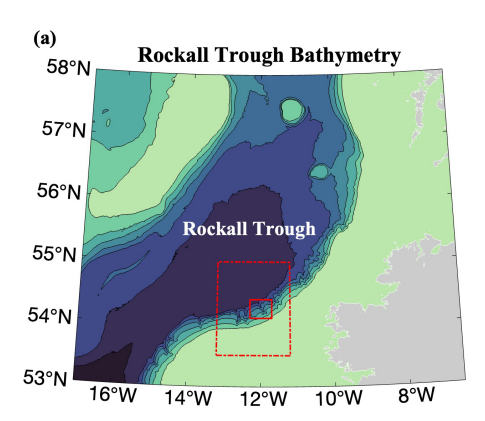
²⁵ Corresponding author: Yuchen Ma, yuchenma@mit.edu

ABSTRACT: Mixing in the ocean abyss sustains the deepest branches of the global overturning circulation, yet the processes that drive deep-ocean mixing remain poorly understood. Recent 27 field measurements in a deep submarine canyon of the Rockall Trough have revealed that intense 28 mixing occurs during strong, vertical shear-generated overturns exceeding 200 meters. These overturning events last only a few hours and occur at different tidal phases across sections of the 30 canyon. We investigate the origin of the shear and its dependence on along-canyon location using 31 a high-resolution numerical simulation and theory. The tidal shear is associated with internal 32 Kelvin waves trapped by the canyon's geometry, whose structure varies along the slope, resulting 33 in distinct tidal phases of shear at different canyon locations. These waves are confined to the depth 34 of the canyon, resulting in stronger shear than the low-mode internal waves that dominate in the ocean interior. Our results suggest that the strong shear associated with standing waves in canyon 36 may play an important role in driving abyssal ocean mixing.

stratification is weakest.

1. Introduction A long-standing puzzle in the study of the ocean's general circulation is how dense abyssal water 39 rises to the surface. Historically, interior mixing has been invoked as the primary mechanism for transforming dense bottom water into lighter upper-ocean water (Munk 1966; Munk and Wunsch 41 1998), but the precise pathways of this transformation remained unclear. More recently, theoretical 42 arguments (De Lavergne et al. 2016; Ferrari et al. 2016; Callies and Ferrari 2018; Drake et al. 2020) have suggested that the diapycnal upwelling of abyssal water is primarily confined to boundary layers along steep topography, while downwelling prevails in the ocean interior. This diapycnal upwelling is closely linked to the detailed processes of ocean mixing along the ocean's bottom boundary, which is not fully understood and the subject of ongoing debate, as recently reviewed 47 by Polzin and McDougall (2022). 48 To test these theoretical arguments and elucidate the physics of boundary layer mixing, the 49 Boundary Layer Turbulence and Abyssal Recipes (BLT Recipes) experiment was conducted in the Rockall Trough (Fig.1a) during 2021–2022, with the goal of measuring mixing processes and 51 water mass transformations in a steep canyon, depicted in Fig.1b. For the purposes of this paper, 52 we will refer to this canyon as the BLT Canyon. Direct evidence of strong upwelling emerged from

the analysis of a dye release experiment. By tracking the center of mass of dye injected near the 54 seafloor (Ruan and Ferrari 2021), the diapycnal (essentially vertical) velocity within the Rockall 55 Trough canyon was found to be on the order of 100 meters per day (Wynne-Cattanach et al. 2024). This rate is approximately 10,000 times greater than the global-average upwelling velocity of about 57 3 meters per year, which is required to sustain the net upwelling of abyssal waters (Munk 1966). 58 Concurrent fine- and microstructure measurements provide compelling evidence that the upwelling is associated with overturns of the density within 200 meters of the seafloor (Naveira Garabato et al. 2025; Alford et al. 2025). A water mass budget analysis confirms that mixing generated 66 by these overturns is consistent with the strong upwelling documented with the dye release mea-67 surements. The overturning events persist for several hours, systematically occurring at the same phase in the tidal cycle. Overturns are detected during the ebb tide at certain locations along the 69 canyon (Wynne-Cattanach et al. 2024) but during the flood tide at others (Naveira Garabato et al. 70 2025). In all cases, the overturns coincide with the "positive-shear" phases of the tide—when



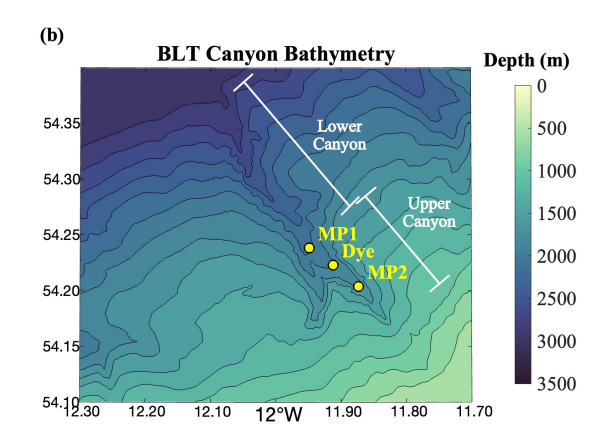


Fig. 1. (a) Bathymetry of the Rockall Trough region. The BLT Canyon area is highlighted with a solid red box, while the simulation domain, discussed in Section 2, is marked with a dotted-dashed line. (b) Bathymetry of the BLT Canyon. The locations of the mooring positions (MP1 and MP2) and the dye release site are indicated by yellow circles. We divide the canyon into upper and lower sections, with the boundary defined at the point where the two canyon branches converge.

Fig. 2 summarizes how tidal phase and shear jointly modulate stratification. In the top-intensified 73 velocity scenario, the strongest tidal velocity is found some distance above the seafloor. During 74 the flood phase, the vertical shear is positive (upslope direction is defined as positive) and the tidal 75 velocity lifts denser water upward more effectively than lighter water, so the vertical stratification 76 decreases. During the ebb phase, the shear reverses, advecting lighter water above denser water and 77 thereby reinforcing stratification. In the scenario where the velocity peaks at the seafloor, the flood tide is associated with negative shear that re-stratifies the column, whereas the ebb tide generates 79 positive shear that erodes stratification. Therefore, it is only the sign of the shear that matters in influencing stratification, not the direction of the flow. 81

Although weaker stratification naturally increases the likelihood of turbulent overturning (Polzin 1996; Alford and Pinkel 2000; Levine and Boyd 2006), the pathway from tidal flow to turbulence is not straightforward. Si et al. (2025) report that the observed tidal shear is too weak to bring the Richardson number (the ratio of the stratification to the low-mode shear squared) below 1/4 or 0

as required to initiate classic shear or convective instabilities, respectively. However, they show that time-dependent tidal shears are parametrically instable at Richardson numbers of order one 87 as observed in the BLT Canyon. An alternative interpretation is that externally generated perturbations to the velocity and buoyancy fields, say by transient waves, bottom drag, and topographic roughness, push the system into a nonlinear regime resulting in density overturns (Alford et al. 90 2025). Three-dimensional nonlinear effects may also be at play: Bellerjeau et al. (2025) analyzed 91 the cross-frequency kinetic energy flux in the BLT Canyon and showed that the tidal kinetic energy is transferred downscale through highly nonlocal interactions on timescales much shorter than predicted by weakly nonlinear wave-wave interaction theories and steady shear instability theories. Finally, high-resolution numerical simulations of tidal shears over a sloping boundary have documented the generation of internal bore-like surges propagating upslope and leading to overturning 96 (Winters 2015). Regardless of the precise mechanism, overturnings span the full depth of the 97 canyon and are associated with positive vertical shear, and hence understanding the along-canyon 98 tidal shear spanning the depth of the canyon is key to interpreting the observations.

The primary objective of this paper is to investigate the origin of the tidal shear observed in the BLT Canyon. A common expectation is that bottom drag, which acts to slow the flow at the sea floor, is responsible for generating this shear. However, as we demonstrate in Section 2, the shear is found to be bottom-intensified at certain locations of the canyon—a finding that contradicts a straightforward bottom-drag explanation. Consequently, an alternative mechanism is required to account for the variability in tidal shear at different locations within the canyon. In this paper, we combine realistic simulation with theoretical calculations to demonstrate that the tidal shear observed in the canyon is driven by standing Kelvin waves confined within the canyon.

106

107

109

110

112

113

Propagating and standing internal tides in submarine canyons have been extensively documented in observations (Petruncio et al. 1998; Kunze et al. 2002; Hall and Carter 2011; Alberty et al. 2017; Waterhouse et al. 2017; Hamann et al. 2021) and in numerical models (Rosenfeld et al. 1999; Carter 2010; Kang and Fringer 2012; Zhang et al. 2014; Aslam et al. 2018; Masunaga et al. 2023). Energy-budget analyses are commonly used to trace the conversion from barotropic—to—baroclinic to eventual breaking and dissipation. Standing (or partly standing) waves are also reported in observations (Martini et al. 2007; Hall et al. 2017). However, existing theoretical descriptions of standing-wave structures are too idealized to be directly compared with the spatially varying shear

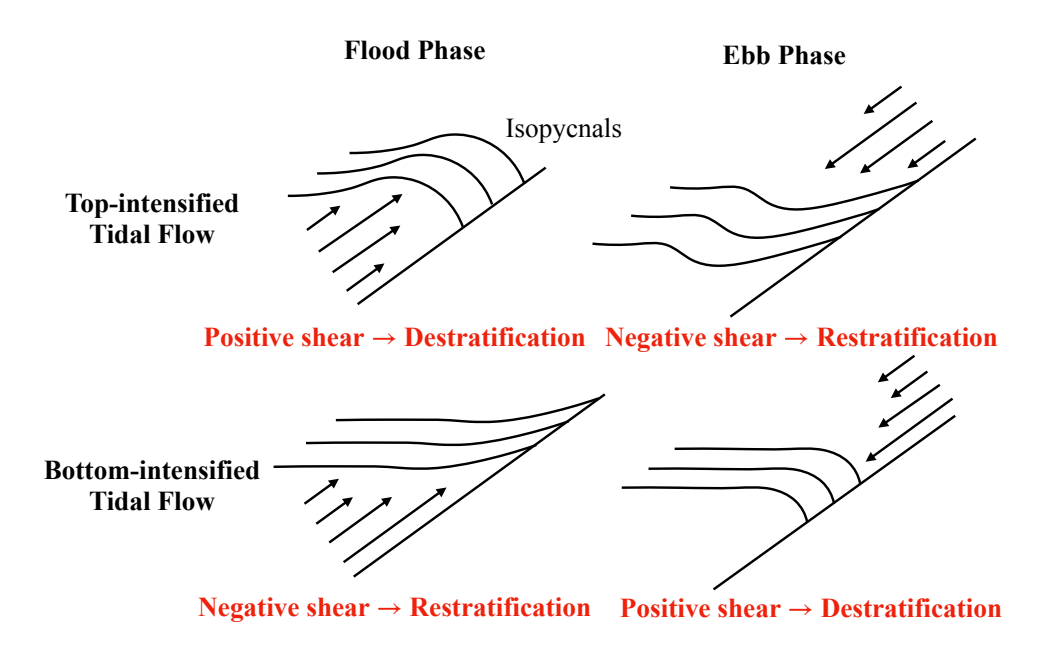


Fig. 2. Schematic illustrating the impact of the tidal shear on stratification and mixing over sloping bathymetry.
In a top-intensified tidal flow (upper row), where the maximum velocity is found above the bottom, stratification
weakens during the flood phase. Conversely, in a bottom-intensified tidal flow (lower row), the stratification is
reduced during the ebb phase as enhanced bottom shear forces lighter fluid beneath denser fluid. Observations
indicate that in both situations, turbulent bursts preferentially occur during periods of strong positive shear,
coupled with weakened stratification.

observed in our field campaigns. In this paper, we develop an analytical model that allows us to 122 compute the structure of the canyon standing-wave modes and compare them with both observations 123 and a realistic simulation. Our focus will be on the low-mode shear spanning the whole depth 124 of the BLT canyon which dominates the shear in observations. In a companion paper (Ma et al. 125 2025), we formulate a more complete theoretical model to study all potential standing wave modes 126 induced by tidal forces within a canyon, but at the expense of simplifications that make a direct comparison to observations less straightforward. Despite this, our analysis corroborates that low 128 modes are more commonly excited, consistent with the findings from observations and numerical 129 simulations presented in this paper.

The paper is organized as follows. First, we present observed examples of tidal shear from the BLT measurements in Section 2. We then conduct high-resolution numerical simulations, incorporating detailed bathymetry and realistic forcing, to replicate the canyon's tidal flow. In Section 3, we introduce a theoretical solution to explain the observed tidal shear in the BLT Canyon and compare it with our realistic simulation. Finally, Section 4 provides a brief discussion and summary.

2. Observations and simulations of tidal shear in the BLT Canyon

a. Observational evidence of tidal shear in the BLT Canyon

The BLT campaign was conducted in a canyon located in the Rockall Trough of the Northeast
Atlantic Ocean (see Fig.1a,b). A series of mooring measurements were carried out between July
and October 2021. We focus on data from two moored profilers (MP): the one-week deployment
at MP1 and the three-month deployment at MP2, with their locations marked in Fig.1b. Additional
moorings were deployed further up the canyon (Wynne-Cattanach et al. 2024), and their shear
patterns are consistent with those from MP2. The mooring data for the BLT campaign used in this
paper are available in Voet et al. (2024).

The along-canyon velocity (the velocity component aligned with the canyon thalweg) measured by the acoustic Doppler current profiler (ADCP) is presented in Fig. 3a,b for selected six-day periods at MP1 and MP2, respectively. The deployment periods of the two moorings do not overlap, with MP1 data collected closer to a neap tide and MP2 data closer to a spring tide. Both measurements exhibit a strong semidiurnal tidal signal of approximately 0.2 m/s, but the MP1 signal shows a slightly greater influence from the diurnal tide. The tidal velocities in the cross-canyon direction (not shown) are an order of magnitude weaker due to the constraints imposed by the canyon lateral walls.

Fig. 3a,b shows that the tidal velocity peaks closest to the seafloor in MP1 and approximately 200 m above the bottom in MP2. These observations correspond to the two scenarios described in the introduction. These differences become even clearer in Fig. 3c–f, where the time series data are phase-averaged over a tidal cycle to highlight the dependence of along-canyon velocity on tidal phases. Fig. 3d,f shows positive shear during the flood phase at MP2 and during the ebb phase at MP1, resulting in decreased dynamical stability in different tidal phases. The goal of this work

is to explain the dynamics that sets the tidal shear, and why this shear has a different structure at different locations along the canyon.

b. Numerical simulation of tidal shear in the Rockall Trough canyon

Diagnosing the physical mechanisms supporting the observed tidal shear from a limited number of observational sites is challenging. Progress can be made by complementing the observations with a simulation with the MIT General Circulation Model (MITgcm, Marshall et al. (1997)) that replicates key aspects of the tidal velocities observed during the measurement period.

1) Configurations of Numerical model

We used a hydrostatic model for our simulations, as our focus is on tidal motions, which have small aspect ratios and low frequencies. The simulation domain, outlined by the dot-dashed line in Fig. 1a, was carefully designed to balance the need for a high-resolution grid with a domain large enough to capture the longest wavelength of the baroclinic tide observed outside the canyon. The model employs a horizontal resolution of 260 m by 220 m $(0.004^{\circ} \times 0.002^{\circ})$ and a uniform vertical resolution of 10 m (300 vertical levels).

The bathymetry of the domain was constructed using high-resolution shipboard multi-beam data (approximately 84 m resolution) collected during the BLT cruises (Wynne-Cattanach et al. 2024), 180 overlaid onto the GEBCO dataset (Weatherall et al. 2023), and interpolated onto the simulation 181 grid. Initial and open boundary conditions for velocities, potential temperature, and salinity were derived from the EU Copernicus 1/12° global reanalysis (Lellouche et al. 2021). Barotropic tides 183 were prescribed at the domain boundaries using TPXO tidal data (Egbert and Erofeeva 2002), 184 incorporating eight tidal constituents (M2, S2, N2, K2, K1, O1, P1, Q1). Atmospheric forcing, including precipitation, wind, and radiation, was applied using data from the JRA-DO dataset 186 (Tsujino et al. 2018). The simulation was run for 40 days to capture a sufficient number of tidal 187 cycles for comparison with the observation periods of MP1 and MP2. It was initialized on June 188 20, 2021, allowing for a 5-day spin-up period before the results could be compared with the MP1 mooring data, which began on June 28, 2021. 190

Subgrid-scale turbulence is represented via Leith hyperviscosity and a vertical mixing closure based on the GGL90 parameterization (Gaspar et al. 1990). Under conditions where denser water

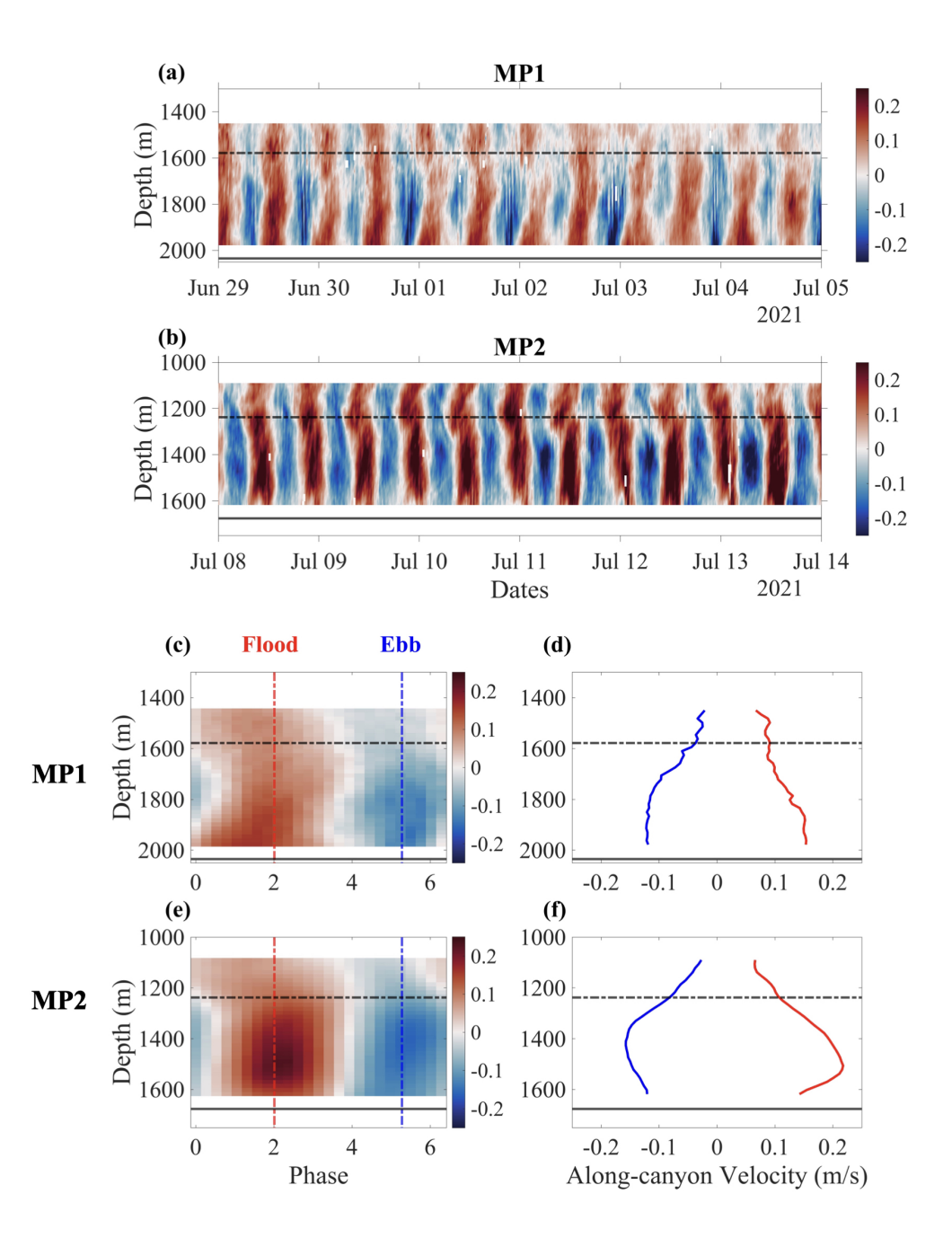


Fig. 3. (a,b): Along-canyon velocity measured by ADCPs at MP1 and MP2 over a six-day period. (c,e):
Along-canyon velocity at MP1 and MP2, averaged over MP2 tidal phases. (d,f): Vertical profiles of along-canyon
velocity at the center of the upslope phase and downslope phase. The exact times are shown as vertical dashed
lines in (c) and (e). The seafloor at MP1 and MP2 is shown as a black solid line, and the canyon top is shown as
a dashed line. The ADCP could not report accurate velocities in the bottom 60 m due to sidelobe interference.

flows over lighter water, the GGL90 scheme prescribes elevated diffusivities and viscosities, thereby capturing enhanced turbulent levels within the canyon to some extent. That said, the key dynamics 194 we are focusing on is the shear that develops in the canyon, which is set by linear dynamics as we 195 discuss below and is not affected by the choice of subgrid-scale closure schemes.

2) Simulation results

197

201

We replicated the deployment of "moorings" in our numerical simulations at the same locations 198 as the actual moorings, MP1 and MP2. We show the comparison of ther vertical profiles of 199 temperature, salinity and stratification in Fig. 4. The profiles at the two mooring sites closely match the observations, in part because the initial conditions and forcing from the Copernicus reanalysis provide a strong constraint. A substantial discrepancy can be seen in the bottom-most 202 two grids at MP1, where the model resolution likely limits fidelity. 203

Simulated and observed tidal velocity profiles are shown in Fig. 5; the simulation closely 209 replicates the along-canyon velocities at MP2 but shows less agreement at MP1. At MP2, the 210 simulation accurately captures both the amplitude and phase of the along-canyon velocities (Fig. 5, 211 last two rows). Notably, the along-canyon velocity peaks at a depth of approximately 1,500 m, which is consistent with observations. This aligns with the "top-intensified tidal flow" scenario 213 described earlier, where positive shear occurs during the flood phases of the tide. In contrast, the 214 simulated tidal flow at MP1 appears more disorganized (Fig. 5, top two rows). While positive shear during some ebb cycles (e.g., around midnight on July 1st, 3rd, and 5th, 2021) is consistent with 216 the observed signal, positive shear is also present during flood phases, which deviates from the 217 observations. This discrepancy likely arises from the complex bathymetry of MP1 (Fig.1b). We show in the next section that the shear is induced by a standing wave pattern constrained by the 219 canyon's topography. Because MP1 sits at the intersection of two canyon branches (see Fig.1b), 220 subtle details in the topography, difficult to capture even with high-resolution multibeam data, 221 become quite important in setting the exact phase structure of the shear. To illustrate this, we compare the tidal shear at MP1* (Fig. 5, third row)—a site located 2 km upstream of MP1 along 223 the canyon thalweg, where the bathymetry is more uniform (shown in Fig. 6). The shear pattern at 224 MP1* agrees more closely with the MP1 observations, suggesting that while the model reproduces

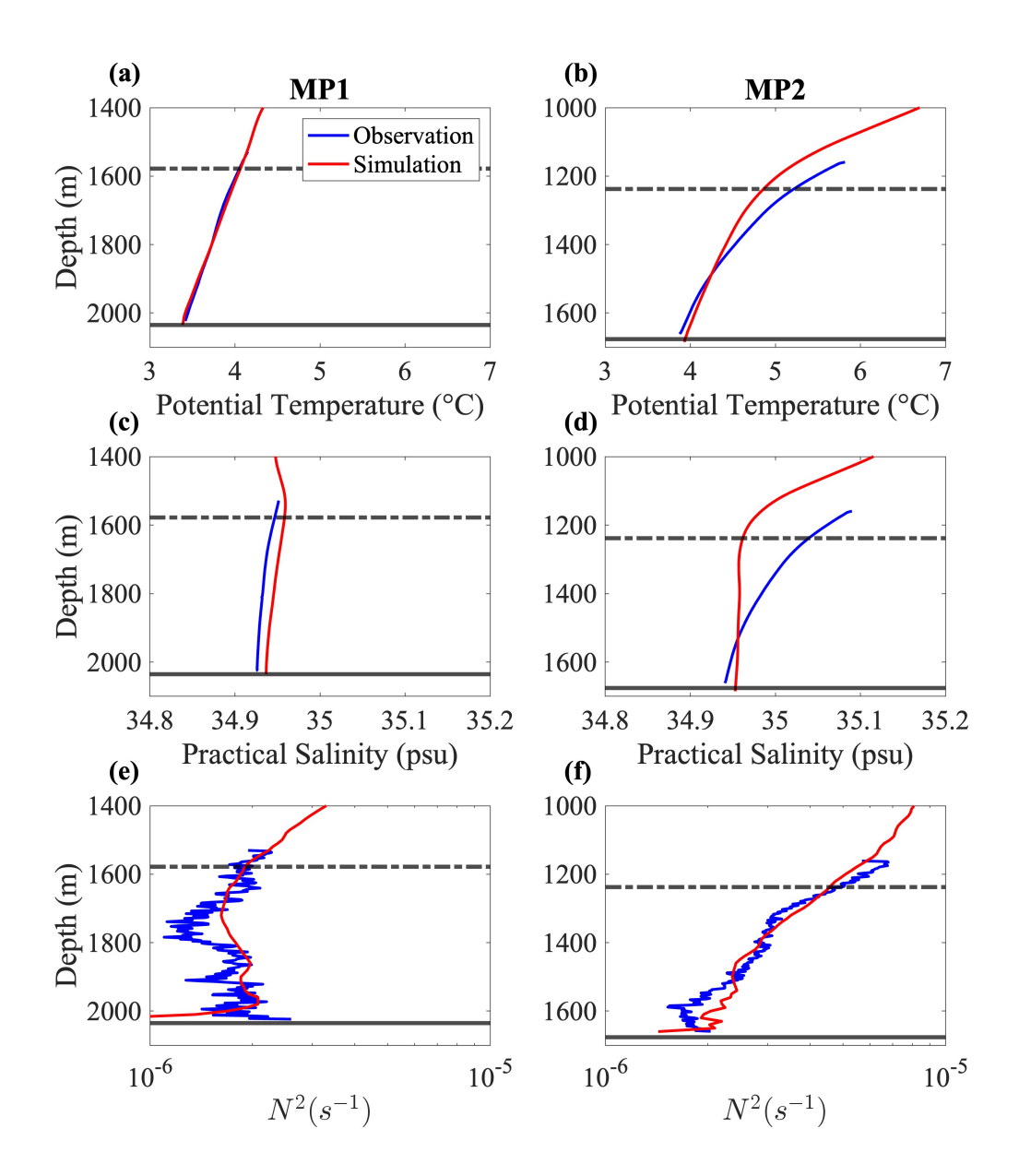


Fig. 4. Vertical profiles of potential temperature, practical salinity and Brunt–Väisälä frequency (N^2) from mooring observations and MITgcm simulations at the MP1 and MP2 sites (see Fig. 1). The seafloor depth is represented a solid black line, and the canyon top as a dashed black line. In both cases, N^2 is calculated using the TEOS-10 package. The profiles shown represent time-averaged values from the moorings (MP1 and MP2) and the simulation.

the different shear regimes, pinpointing their exact location proves challenging given the canyon's complex bathymetry.

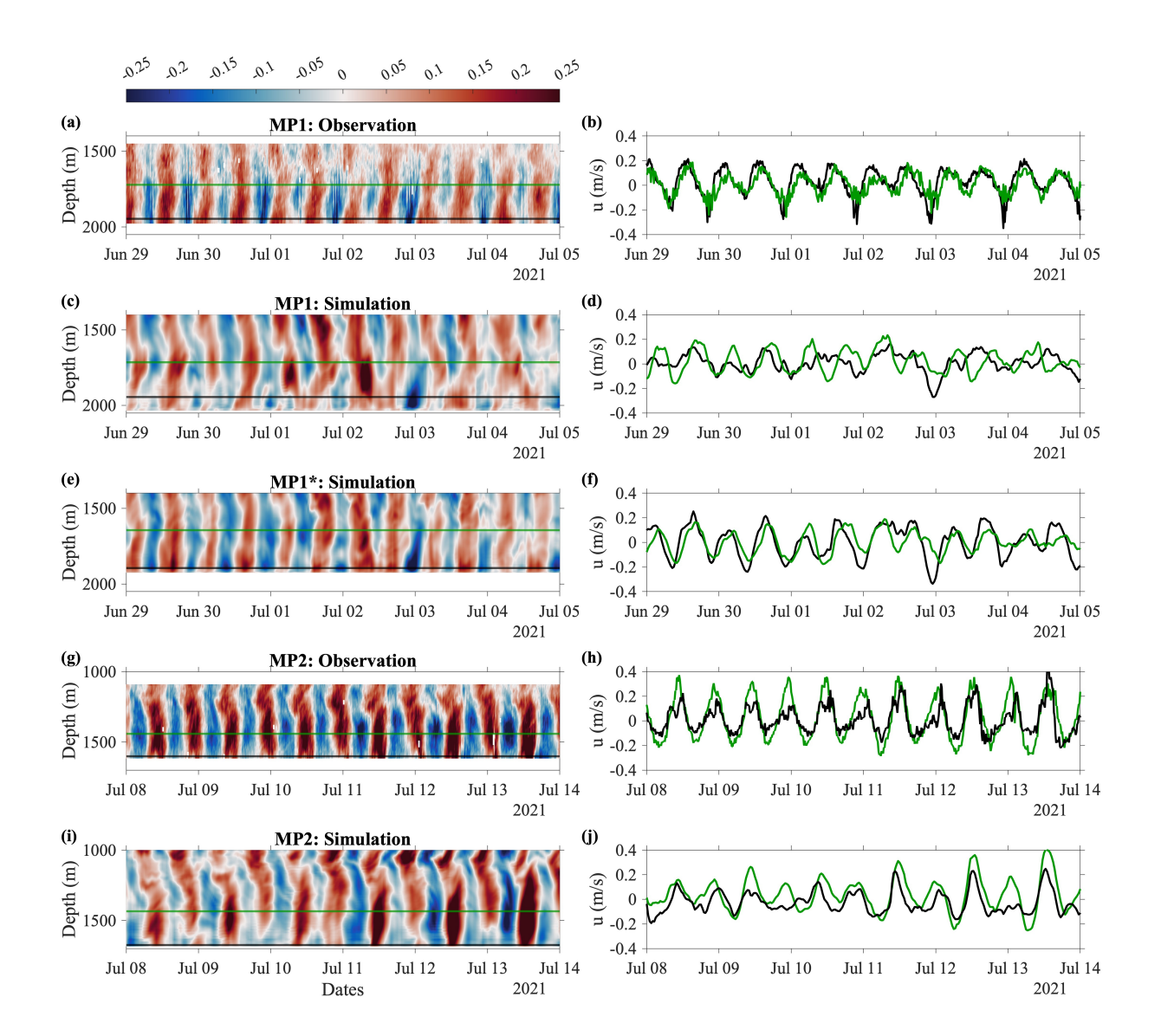


Fig. 5. Left panels: Along-canyon velocity from ADCPs and from a realistic MITgcm simulation, at the MP1 and MP2 position in Fig. 1 respectively. The simulated along-canyon velocity at the MP1* position, located 2 km upstream of MP1, is also shown to be compared with observed tidal shear. Right panels: Time series of along-canyon velocity at the two depths, one close to the bottom (black horizontal line in left panel) and the other 300 meters above it (green horizontal line in left panel). Velocities are bottom-intensified tidal flow at (observations) and MP1* (simulation) and top-intensified flow at MP2 (observations and simulation).

To gain deeper insights into the tidal flow within the canyon, we extend the numerical "mooring" array to each available point along the canyon thalweg in our simulation. This enables us to explore the spatial structure of tidal velocities more comprehensively. The individual profiles used to define the canyon thalweg are marked as red dots in Fig. 6a. By connecting these discrete positions, the two-dimensional bathymetry is reduced to a one-dimensional representation that follows the canyon thalweg. Along-canyon distance is then used to indicate the relative positions of these profiles within the canyon. Lastly, Fig. 6b shows a representative example of the cross-canyon V-shaped bathymetry at the location marked with a thicker dot in Fig. 6a. We define the height of the canyon sidewalls using thresholds of 3 km and 5 km, corresponding to stricter and looser definitions, respectively.

234

235

236

238

239

241

242

248

249

250

Using the "mooring" array, we can construct a 2D velocity field u(x, z, t) as a function of along thalweg, x, depth, z, and time t. The velocity field can be decomposed into frequency components

$$u(x,z,t) = \sum_{n} A_{u,n}(x,z) \cos(\omega_n t - \phi_{u,n})$$

$$= \sum_{n} A_{u,n}(x,z) \operatorname{Re} \left(e^{-i(\omega_n t - \phi_{u,n})} \right)$$

$$= \frac{1}{2} \sum_{n} A_{u,n}(x,z) \left(e^{i(\omega_n t - \phi_{u,n})} + e^{-i(\omega_n t - \phi_{u,n})} \right)$$
(1)

where the ω_n are the set of discrete frequencies that fit in the time interval being considered, the $A_{u,n}(x,z)$ are the amplitudes of each frequency mode, and the $\phi_{u,n}$ are their phases. We are interested in isolating the tidal component with $\omega_n = \omega_{M2}$ which drives the overturning events observed in the canyon. This is achieved by complex demodulation of the signal. i.e. by multiplying the velocity field by $e^{-i\omega_{M2}t}$ and integrating in time over n tidal cycles,

$$\frac{2}{nT} \int_0^{nT} u(x, z, t) e^{-i\omega_{M2}t} dt = A_{u, M2}(x, z) e^{-i\phi_{u, M2}}.$$
 (2)

From now on, we will drop the subscript M2 from amplitudes and phases, because we focus exclusively on that tidal component. The complex demodulation integral is computed on 60 tidal cycles of length T=12.42 hours and $\omega=\frac{2\pi}{T}$. Similar definitions apply to the M2 tidal component of the buoyancy field, $A_b(x,z)$ and $\phi_b(x,z)$, and the baroclinic pressure field, $A_p(x,z)$ and $\phi_p(x,z)$, which will be discussed later.

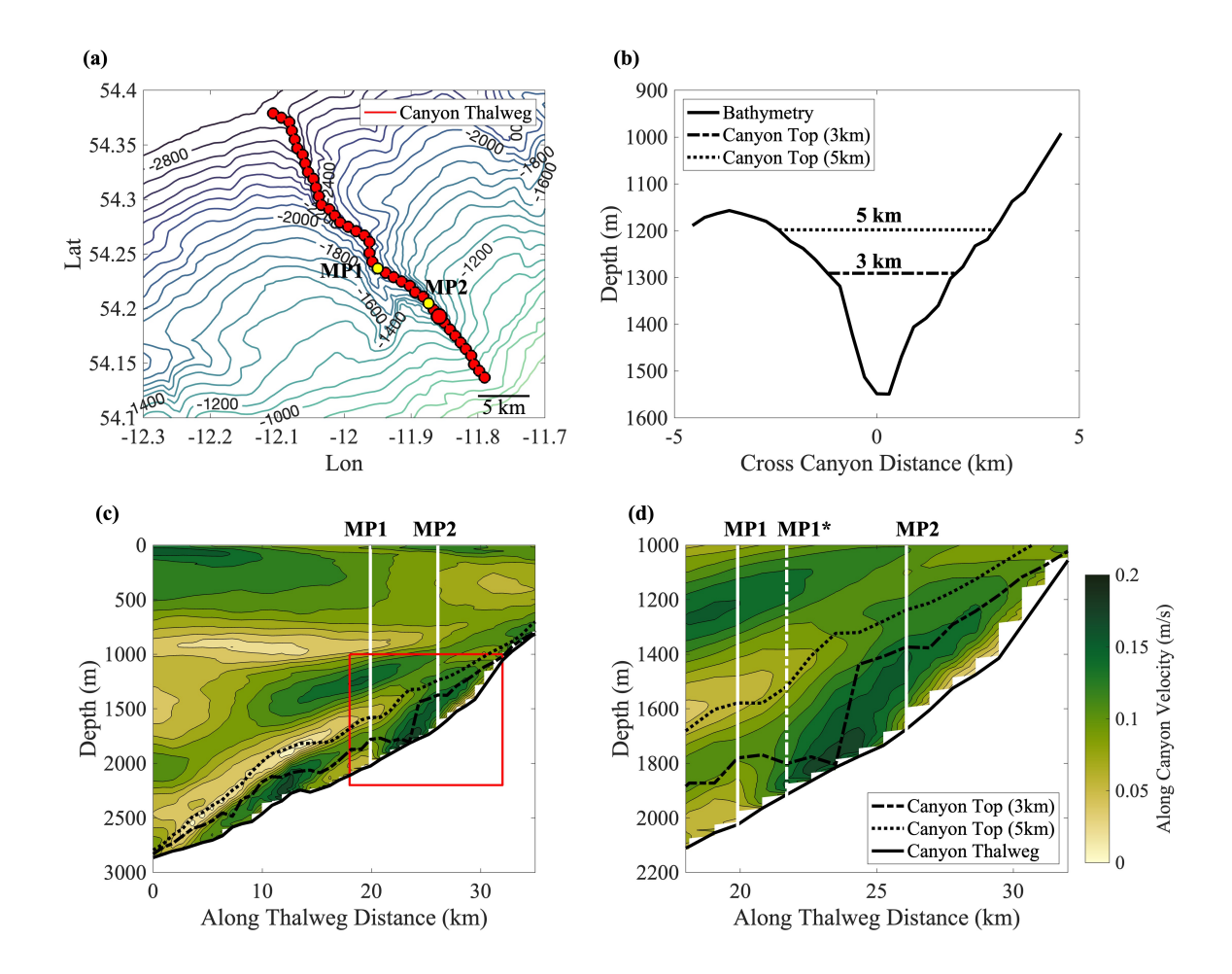


Fig. 6. (a) The BLT Canyon bathymetry. The red dots represent an array of numerical "moorings" along the thalweg of the canyon. (b) Cross-canyon topography at the position of the larger red dot in panel (a) illustrates the two definitions of canyon top based on a width of 3 km and 5 km, respectively. (c) Amplitude of the M2 tidal velocity along the section, A_u . (d) Same as (c), but zoomed in on the red-box region of (c).

The amplitude $A_u(x,z)$ of the tidal velocity is shown in Fig. 6c for the whole canyon and in Fig. 6d for the section of the canyon where the BLT moorings were deployed. The locations of MP1 and MP2 are indicated with white vertical lines. At MP2, A_u peaks at around 1500 m depth and about 200 m above the seafloor. At MP1, the velocity peaks above the seafloor, inconsistent with the observations (Fig. 3), but a bottom-intensified tidal flow is seen a few kilometers downstream at MP1* (denoted by the white dashed line).

This suggests that the simulation qualitatively captures the variations in shear structure at different canyon locations. The variation in tidal phase arises from the tilted structure of the M2 tidal amplitude, as shown in Fig. 6d, with angles steeper than the underlying bathymetry. We investigate what physics sets this structure in the next section.

271 c. Investigating the origin of shear through numerical simulation

We verified that the shear pattern observed in the data is qualitatively captured by our realistic simulations. This prompts us to explore the dynamics that generate the tidal shear through a detailed analysis of the numerical simulation.

One may may be tempted to attribute the tidal shear to the effects of bottom drag. While bottom-friction-induced flow can generate shear within the bottom boundary layer (Lorke et al. 2005; Umlauf and Burchard 2011), the shear observed at the BLT moorings spans a much larger vertical scale, on the order of a hundred meters. More importantly, bottom drag acts to slow down the flow along the sea floor and is inconsistent with the bottom-intensified tidal flow observed in both the observations (MP1 mooring) and simulations (MP1* Position).

This leads us to the hypothesis that the tidal shear originates from an internal wave pattern driven by the tidal forces acting in the canyon. To test this hypothesis and identify the origin of the shear in the model, we compute the vertically integrated along-canyon shear budget between two selected depths:

$$\frac{1}{|z_{1}-z_{2}|}\overline{u}_{t}|_{z_{2}}^{z_{1}} = \frac{1}{|z_{1}-z_{2}|} \left[\underbrace{-\overline{p_{x}}|_{z_{2}}^{z_{1}}}_{\text{Pressure Gradient Term Coriolis Term}} + \underbrace{f\overline{v}|_{z_{2}}^{z_{1}}}_{\text{Shear Tendency}} + \underbrace{(-\overline{(uu)_{x}} - \overline{(uv)_{y}} - \overline{(uw)_{z}})|_{z_{2}}^{z_{1}}}_{\text{Advection Term}} - \underbrace{\overline{v_{1}}|_{z_{2}}^{z_{1}} + \overline{(\text{Leith Dissipation})}|_{z_{2}}^{z_{1}}}_{\text{Diffusion Term}} \right]_{z_{2}}^{z_{1}}$$
(3)

Here, the overbar denotes a 30-minute running average. z_1 and z_2 are two selected depths between which there is a strong shear. At MP1, where the tidal flow is bottom-intensified with a maximum roughly 30 m above the bottom, we chose $z_1 = 1700$ m and $z_2 = 1,900$ m. At MP2, we selected $z_1 = 1,500$ m, where the tidal velocity maximum, and $z_2 = 1,690$ m, the bottom-most numerical grid. $\tau = -vu_z$ is the parameterized viscous vertical momentum flux. Note that at MP2, the vertical

dissipation term τ_z in the bottom-most grid cell also includes the contribution from the quadratic bottom drag. To remove high-frequency noise and isolate the tidal signal at frequencies close to the M2 tide, we apply a band-pass filter to the shear tendency terms—the width of the filter in frequency space is shown in the shear spectra in Fig. 7a, b.

The band-passed shear budget in Fig. 7c,d reveals clear patterns: u_z is predominantly driven by the pressure gradient and Coriolis terms. In contrast, the advection and dissipation terms contribute minimally to the shear budget and are generally out of phase with the shear tendency. This analysis provides compelling evidence that the canyon tidal shear observed in the numerical simulations is primarily generated by linear wave dynamics.

Further inspection of the contributions from the pressure gradient and Coriolis terms in Fig. 7e,f reveals that the dominant factor driving the tidal shear is the pressure gradient term. As we will discuss below, this dominance is a characteristic signature of Kelvin waves, whose cross-canyon motion is strongly constrained by the canyon walls.

Although we demonstrated that tidal shears are dominated by linear dynamics, we still need to understand the characteristics of these waves. In particular, we need to assess whether these waves are standing waves or propagating waves. To this end, we plot in Fig. 8 the phases of the tidal oscillations at each spatial location along the 2D thalweg transect, following the definition in Eq. (2). Both ϕ_u and ϕ_b are presented. The key difference is that ϕ_b reflects only contributions from baroclinic tides, whereas ϕ_u is influenced by both barotropic and baroclinic tides. If the waves in the canyon were propagating, with a wavelength comparable to the canyon's height, one would expect the phase to change rapidly inside the canyon. On the other hand, if the waves were standing, there should be small phase differences inside the canyon.

311

312

314

315

317

318

319

321

322

324

325

Focusing on the red box region in Fig. 8, where the BLT moorings were deployed, it is clear that the tidal phases change minimally, indicating the presence of standing waves. In the next section, we will focus on this region and demonstrate that standing waves can only be supported in this region, where the canyon slope transitions from subcritical to supercritical relative to Kelvin wave dynamics. Further down the canyon, consistent with the theory, the wave signals exhibit propagating features, and the group velocity (perpendicular to the phase velocity) is directed toward deeper parts of the canyon. In this area, the slope remains subcritical to Kelvin wave characteristics, and the theoretical framework presented in the next section does not apply. Because our primary goal

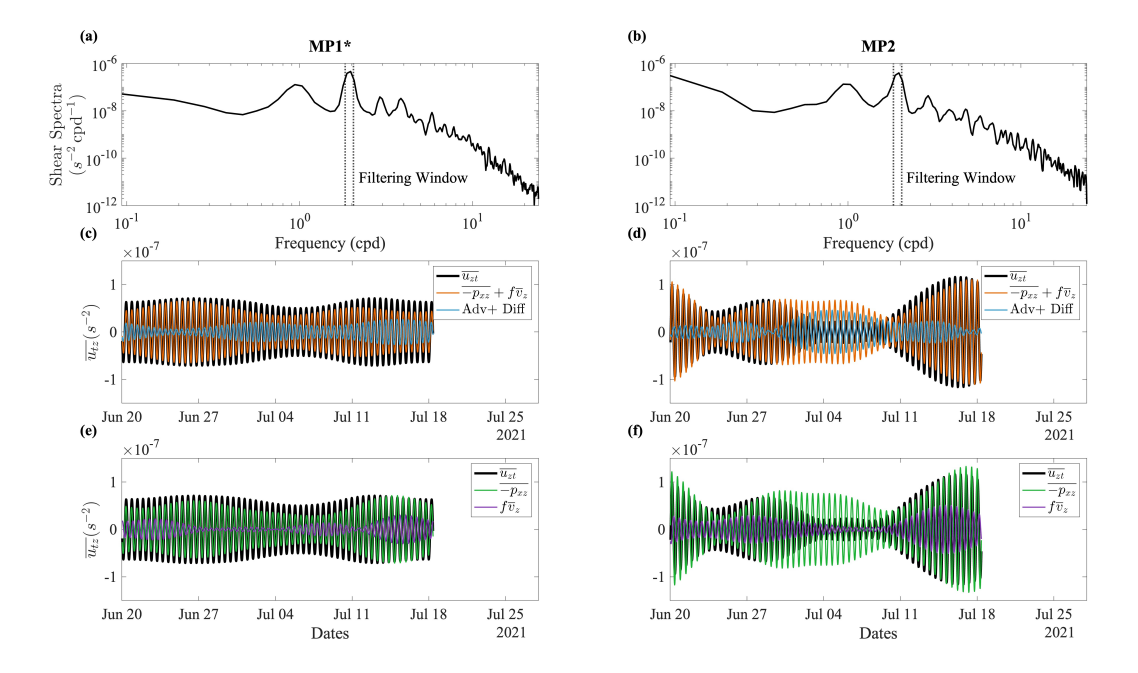


Fig. 7. Budget analysis of the mean shear at the MP1* and MP2 positions, band passed near M2 tidal frequency. (a,b) Power density spectrum of the along-canyon velocity shear u_{tz} . The with of the filtering window is shown by the vertical dotted lines. (c,d) Shear tendency (black lines), sum of Pressure Gradient and Coriolis terms (red lines; wave contribution), and sum of Advection term and Diffusion terms (blue lines; nonlinear contribution)–see Eq.(3). (e,f) Shear tendency, Pressure Gradient, and Coriolis terms.

is to explain the tilted structure in the upper canyon, we do not delve further into these propagating features.

3. Standing wave structure in the BLT Canyon

303

304

305

306

307

332

In this section, we solve for the standing waves that fit in the upper BLT Canyon and their associated shear pattern.

a. Simplification of the upper BLT Canyon using a two-slope model

We begin by simplifying the BLT Canyon geometry to allow analytical progress. The crosscanyon velocity, being blocked by steep lateral canyon walls, is much smaller than the along-canyon one (Van Haren et al. 2024); the leading-order along-canyon x-momentum budget is $u_t \sim -p_x$ (see Fig. 7c) and the cross-canyon y-momentum budget is $fu = -p_y$. These balances hold at all phases

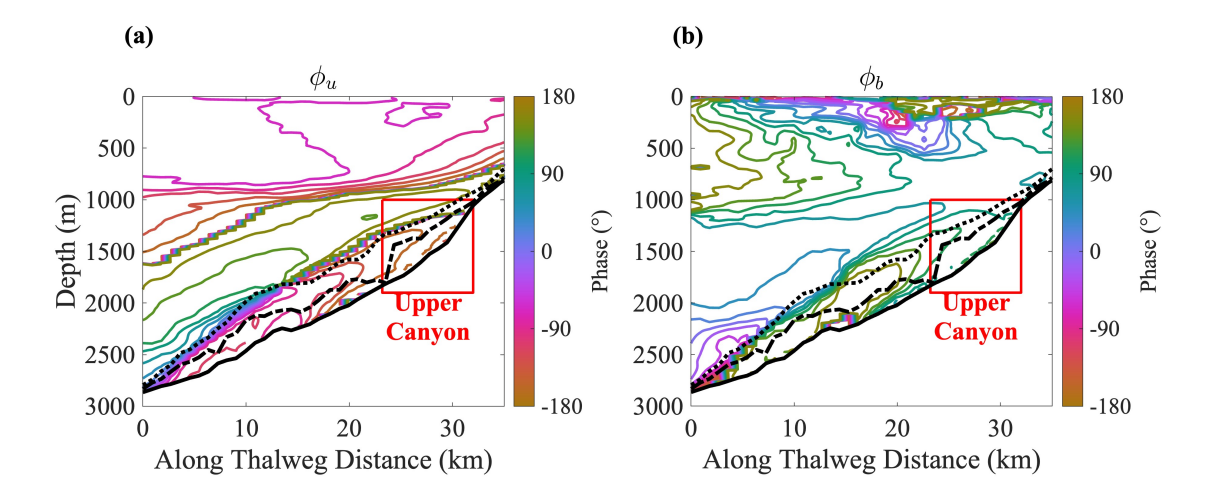


Fig. 8. Contour plot of phases of the M_2 component of vertical variation and ϕ_u buoyancy variation, ϕ_b , plotted in the vertical transect along the canyon thalweg.

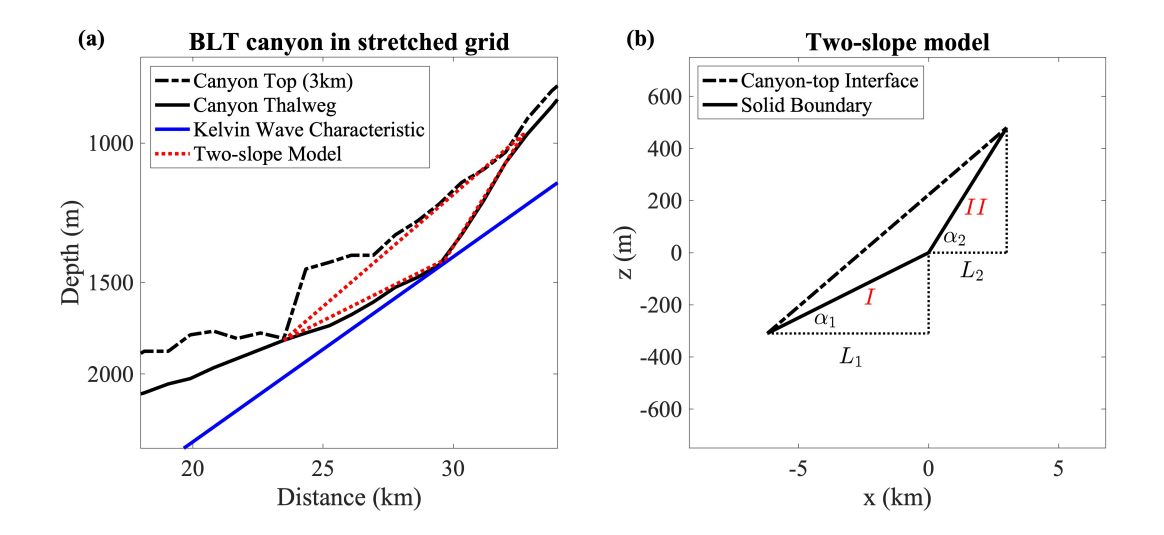


Fig. 9. (a) Canyon thalweg (black continuous line) and canyon top (black dashed line) on a stretched grid. The red line indicates the Kelvin wave characteristics for comparison with the slope. (b) The simplified two-slope model with dimensions that best fit the BLT Canyon.

of the tidal period (not shown) and are telltale signatures of internal Kelvin waves. Internal Kelvin waves are the dominant wave modes in narrow canyons (Webb and Pond 1986; Grimshaw

et al. 1985; Swart et al. 2011). Unlike coastal Kelvin waves—which can only propagate in one direction—the presence of two canyon walls permits bi-directional propagation (Taylor 1922; Chen and Allen 1996; Pratt and Whitehead 2007). The two Kelvin-wave branches decay away from the lateral canyon walls as $e^{\pm y/L_d}$, where $L_d = \omega/(fk)$ is the deformation radius for horizontal wavenumber k. When L_d greatly exceeds the canyon width, the y-dependence is weak and the solution is effectively a two-dimensional wave solution without any y-dependence (Grimshaw et al. 1985; Le Souëf and Allen 2014). In our case, $L_d \sim O(10 \, \mathrm{km})$ for the low-order Kelvin modes, much larger than the $\sim O(1\,\mathrm{km})$ cross-canyon span. To leading order, we therefore approximate the 3D problem as a 2D x-z system.

We further simplify the problem by employing a stretched vertical coordinate following, for example, Leaman and Sanford (1975):

$$\tilde{z} = \int_{-3000 \text{m}}^{z} \frac{\overline{N(z')}}{N_0} dz' \tag{4}$$

where \tilde{z} and z are stretched and original coordinates. $\overline{N(z)}$ is the time and horizontally averaged stratification profile in the simulation, and $N_0 = 1.98 \times 10^{-3} \, \mathrm{s}^{-1}$ a reference stratification. This transformation is equivalent to a WKB approximation, and we verified that it is an accurate representation of the true vertical modes based on the full N(z) profile. By stretching the vertical coordinate, the curved Kelvin-wave characteristics—induced by the nonuniform stratification—are transformed into straight lines, thereby greatly simplifying the theoretical analysis. Fig. 9a shows the 1D profiles of the canyon top and thalweg as functions of along-thalweg distance in the stretched coordinates. The plot reveals a sharp transition in the canyon bottom slope near near 30 km from the canyon head.

To capture the dominant geometric features of this section of the BLT Canyon, we idealize the topography as two straight lines, one with a subcritical slope followed by one with a supercritical slope represented by the red dotted line in Fig. 9a and in greater detail in Fig. 9b. We denote the subcritical slope as α_1 ($\alpha_1 < \alpha_c$) and the supercritical slope as α_2 ($\alpha_2 > \alpha_c$), while $\alpha_c = \omega/N_0$ represents the Kelvin wave characteristic slope. The horizontal extent of the subcritical and supercritical sections are indicated by L_1 and L_2 , respectively. The specific parameters for the two-slope model used to represent the actual BLT Canyon are summarized in Table 1.

L_1	L_2	α_1	α_2	α_c	N_0
6.2km	3km	0.05	0.16	0.0735	$1.98 \times 10^{-3} s^{-1}$

TABLE 1. Key parameters for the two-slope model to capture the shape of the BLT Canyon.

b. Standing wave modes of the two-slope model

We can now solve for the standing wave solutions supported by the idealized two-slope model.

We use a streamfunction ψ to represent the 2D velocity (with $u = \psi_z$, $w = -\psi_x$). The linearized equation of motions then reduce to

$$\begin{cases} \psi_{zt} = -p_x \\ 0 = b - p_z \\ b_t - N_0^2 \psi_x = 0 \end{cases}$$

$$(5)$$

which can be simplified to a single equation for ψ

$$\psi_{zztt} + N_0^2 \psi_{xx} = 0 \tag{6}$$

For wave motions at the tidal frequency, the streamfunction can be represented as $\psi(x,z,t) = \hat{\psi}(x,z)e^{-i\omega t}$ (\hat{u} , \hat{p} , \hat{b} are defined accordingly), and thus

$$\hat{\psi}_{xx} - \alpha_c^2 \hat{\psi}_{zz} = 0 \tag{7}$$

where $\alpha_c = \omega/N_0$ is the dispersion relation of both 2D internal waves and Kelvin waves under hydrostatic approximation. The streamfunction $\hat{\psi}$ must vanish at the two solid canyon walls, i.e. $\hat{\psi} = 0$. As detailed in the Appendix, these boundary conditions confine the interior solution to a set of discrete standing-wave modes. The open boundary, in contrast, determines the amplitudes of the modes that are actually excited. At the open boundary, the pressure must be continuous. Outside the canyon, this pressure consists of (i) the imposed barotropic and baroclinic tidal forcing and (ii) the pressure carried by waves radiated from the canyon top interface into the open ocean. Matching the two provides a linear relation that sets the amplitude of each interior mode for a given forcing. The details of the internal Kelvin-wave excitation are not the main focus of the present paper and

are treated in an accompanying paper Ma et al. (2025), which uses a no-slope geometry to make analytical progress at the expense of making comparison to observations less transparent. For present purposes, their analysis confirms that the gravest standing modes are preferentially excited in the canyon when the external forcing has scales much larger than the canyon length itself. This is also demonstrated in the more empirical forthcoming analysis.

Fig. 10 presents the normalized streamfunction and along-canyon velocity for the three gravest eigenmodes obtained from the wall boundary conditions derived in the Appendix. The lowest-order mode depicts a simple sloshing motion that alternates between moving toward and away from the canyon head. Higher-order modes contain additional nodes, so their streamfunction fields display progressively finer structure with more circulation cells filling the cross-section.

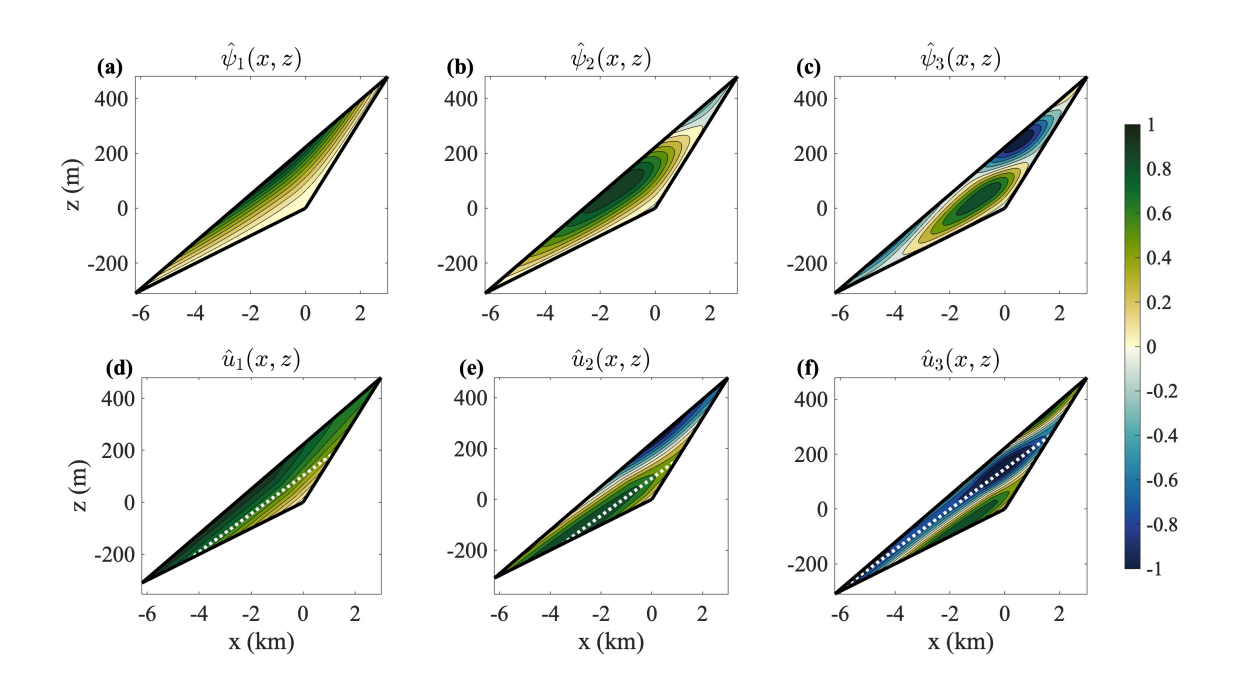


Fig. 10. Streamfunction (a-c) and along-canyon velocity (d-f) of the three gravest eigenmodes in the two-slope model. The Kelvin wave characteristics are shown in white-dashed lines in (d-f) for comparison purposes. Note that standing wave structures do not have phase variations so that both $\hat{\psi}$ and \hat{u} can be defined as real fields.

In Fig. 10 (d-f), we observe a consistent pattern for all these wave modes: the velocity patterns follow the Kelvin wave characteristic slopes well. Since the slope of Kelvin waves is steeper than the gentler slope $\alpha_c > \alpha_1$, the peak in tidal velocities moves further away from the seafloor toward the shallower sections of the canyon. This pattern is consistent with both field observations and

numerical simulations, where the tidal flow peaks near the seafloor in the deeper section of the canyon, but aloft in the shallower section.

404 c. Comparison with the realistic simulation

We argued that the BLT Canyon geometry can be approximated with a two-slope configuration, and we described how to calculate the modal structure of standing waves in such a canyon. To test this interpretation, we now compare the predicted structure of the gravest eigenmode of standing waves with the results from our realistic simulation. As we have previously shown in Fig. 4, the simulated stratification matches the observed profile in the canyon well, making the comparison possible.

We start by analyzing the spatial structure of the M2 wave fields in our realistic simulations. The relevant fields associated with waves include the along-canyon velocity u, buoyancy b, and the pressure anomaly relative to the spatial-mean sea surface height variations, p'(x, y, z, t), which is defined as:

$$p'(x, y, z, t) = p(x, y, z, t) - g\overline{\eta(x, y, t)}_{x, y},$$
(8)

Removing the spatial average of the pressure caused by sea surface height variations eliminates the spatially independent part of the flow, which does not contribute to wave excitation in the canyon, allowing us to focus on the spatially dependent variations of the tidal pressure.

In Fig. 11a-c, we show the amplitude of the tidal components of velocity, A_u , buoyancy A_b , and the pressure anomaly field normalized by the reference density of 1000 kg/m³, A_p/ρ_0 , following the same M2 complex demodulation signal described earlier in Eq. (2). These figures reveal that the maximum amplitudes of the tidal components for velocity, buoyancy, and pressure occur at different heights above the seafloor in different sections of the canyon.

In Fig. 11g-i, we plot analytical solutions for the amplitudes of A_u , A_b , and A_p for the lowest-order Kelvin wave mode, which are simply the absolute values of $|\hat{u}|$, $|\hat{b}|$ and $|\hat{p}|$ in the linear model. These theoretically predicted patterns can be directly compared with the zoomed-in view of the two-slope region of the simulation fields shown in Fig. 11d-f: the lowest-order internal wave mode reasonably matches the patterns observed in the realistic simulation. The along-canyon velocities peak at the seafloor on the deeper side of the canyon, the buoyancy fluctuations are largest on the shallow side near the top of the canyon, and the pressure anomalies peak near the critical slope of

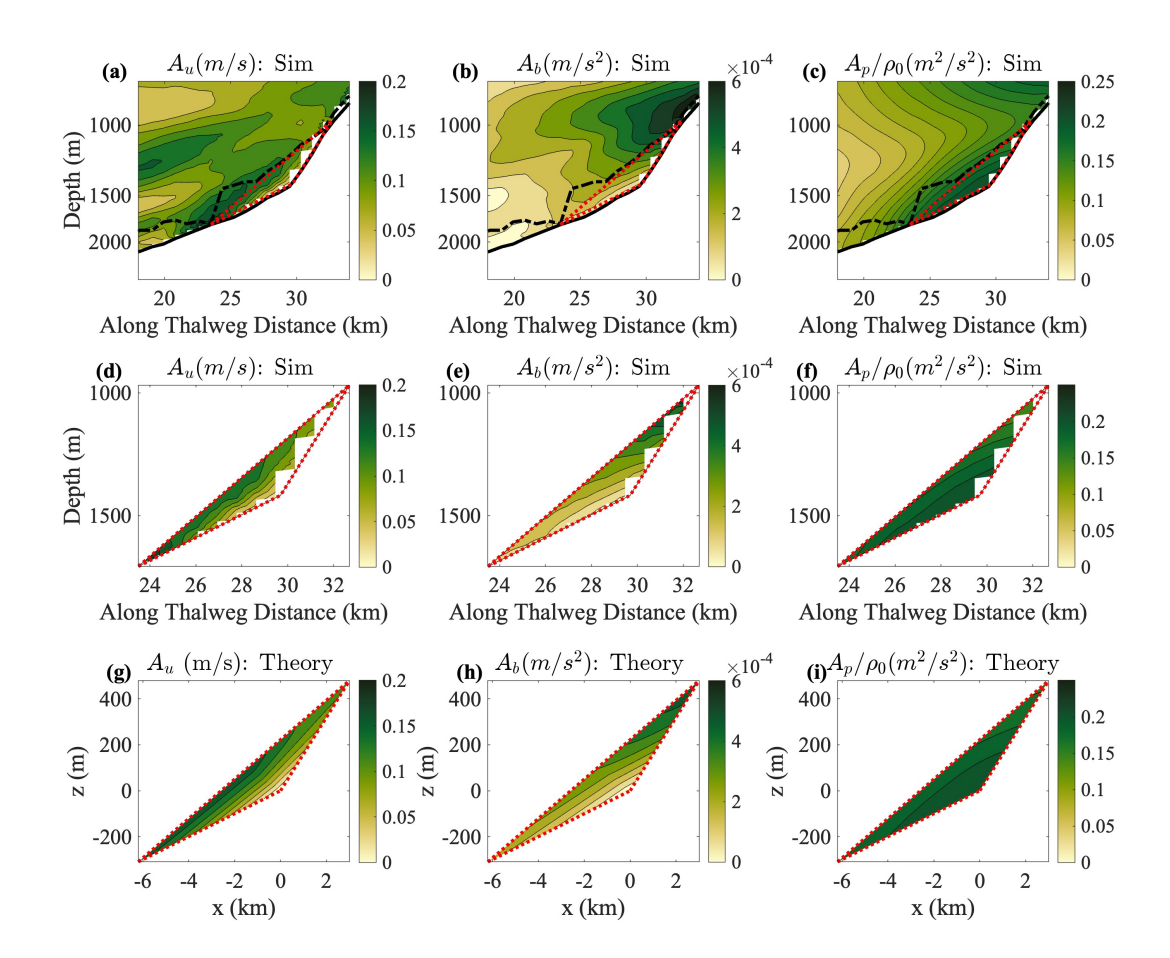


Fig. 11. (a-c): Amplitude of the M2 component of along-canyon velocity A_u , buoyancy A_b , and pressure anomaly p in the realistic simulation in the stretched grid. (d-f): Same as (a-c) but zoomed in for the red-dashed region. (g-i) Lowest-order mode of the two-slope model, with mode amplitudes scaled to match the amplitude of the along-canyon velocity in the simulation. The same colorbars and contour plots are used to visualize the fields from both simulations and theoretical predictions. The same aspect ratio is applied to all these figures.

the canyon. Most importantly, the top-intensified velocity on the shallower end of the canyon and bottom-intensified velocity on the deeper side are consistent with both theory and observations.

These comparisons provide support for the claim that the tidal shear observed in the canyon is caused by a standing internal Kelvin wave.

The standing internal Kelvin wave observed in the BLT Canyon appears to be forced by both the barotropic and baroclinic tides. Fig. 6c shows a pronounced baroclinic signal outside the canyon,

with tidal-velocity amplitudes peaking near 1500 m. This external baroclinic tide was observed by a two-day pilot ADCP survey in September 2019 (Huvenne and Thornton 2020). It seems likely that such a strong baroclinic component should exert a substantial pressure forcing at the canyon top interface.

To gauge the relative importance of barotropic and baroclinic components, we have conducted an 445 additional simulation (not shown) using the same configuration but restricted to a smaller domain 446 (approximately 35 km by 30 km, whereas the original domain is approximately 130 km by 165 km) 447 centered on the canyon region. In this reduced-size model the barotropic tide is still prescribed 448 through TPXO forcing, yet the resulting tidal velocity is only about 0.1m/s—roughly half of that 449 obtained in the larger-domain run and in the observations. This is likely because the reduced size 450 domain is too small to fit the first baroclinic mode, whose wavelength is about 70 km for a 2000 451 m water column. We are thus led to conclude that both barotropic and baroclinic tides drive the 452 standing waves observed in the upper BLT Canyon. 453

4. Discussions and Conclusions

Recent observations suggest that the strong net upwelling of water along a submarine canyon in the Rockall Trough results from overturns coinciding with positive tidal shear once per tidal cycle.

This tidal shear tends to become positive at different tidal phases in various sections of the canyon,

leading to overturning during either the flood or ebb phases.

In this work, we explored the physics leading to the observed tidal shears. By analyzing the output of realistic simulations that reproduce the spatial and temporal patterns of tidal shear, we showed that the canyon geometry supports standing internal tides, whose dynamics are predominantly controlled by pressure gradient forces.

To investigate the internal tide structure within the canyon, we simplified the complex canyon bathymetry into an idealized 2D model consisting of a subcritical slope and a supercritical slope, and solved for the standing internal Kelvin wave modes. Notably, the lowest-order mode of the idealized model accurately captures the observed spatial distribution of shear and resembled the wave patterns seen in realistic simulations. Consequently, these analyses support the conclusion that tidal shear in the canyon is driven by internal standing Kelvin wave modes excited by a combination of baroclinic and barotropic tides.

In the submarine canyon sampled during the BLT experiment, tidally driven internal Kelvin waves induce strong shear that modulates the local stratification. Even though the shear does not appear to be strong enough as to bring the Richardson number below 1/4 or 0 (Si et al. 2025) –the conditions for shear and convective instabilities respectively – the shear is likely to trigger turbulent overturning events either through parametric instabilities due to the time dependence of the shear (Si et al. 2025) or through nonlinear destabilization of the boundary layer (Winters 2015). These overturns generate strong mixing and support the strong upwelling of about 100 meters per day captured in the BLT dye-release experiment (Wynne-Cattanach et al. 2024).

Our analysis of the spatial structure of the shear along the canyon has an additional important implication for the distribution of turbulent mixing along the canyon. We demonstrated that the internal Kelvin waves generate positive shear at different phases of the tidal cycle along the canyon axis. We thus expect that at any single time, patches of turbulence will be confined to regions where the shear is positive. These localized patches result in lateral convergences and divergences of buoyancy flux along the canyon axis, promoting the exchange of waters between the canyon and the ocean interior as discussed in Wynne-Cattanach et al. (2025).

Although our analysis focuses on the standing internal Kelvin waves trapped within the upper canyon to explain the difference in shear at different locations, propagating internal Kelvin waves emerge in the deeper, subcritical portion of the canyon. In our simulation, these propagating modes have vertical scales comparable to the canyon depth and thus generate vigorous tidal shears within the canyon. While a detailed analysis of the propagating waves is beyond the scope of this study, it seems safe to speculate that the tidal excitation of both standing and propagating waves generates strong shears along the ocean seafloor in different sectors of the BLT canyon. (We focused on standing waves because they dominate the shear at the locations sampled during the BLT campaign.) Both kind of waves result in larger shears than those associated with the low-mode tides in the ocean interior.

The internal-tide-induced shear identified in the BLT Canyon probably occurs in other canyons as well, making canyons likely hotspots for shear-driven mixing and the upwelling of dense waters.

Our analysis further indicates that narrow canyons whose thalweg geometry is near critical to internal Kelvin waves are especially efficient at generating strong shears. It has been reported that canyons cutting through continental slopes often have critical slopes, likely because oscillatory

bottom stresses from internal tides erode the seabed and help align the mean gradient with the 500 internal-wave ray angle (Cacchione et al. 2002). Therefore, the excitation of standing waves 501 provides an additional, potentially significant source of enhanced turbulent mixing in submarine 502 canyons, supplementing known processes like canyon focusing and the convergence of internal waves (Gordon and Marshall 1976; Hotchkiss and Wunsch 1982), internal wave reflection and 504 steepening (Kunze et al. 2002; Alberty et al. 2017), breaking internal lee waves (Zhao et al. 2012; 505 Alford and MacCready 2014), and hydraulic jumps (Key 1999; Wain et al. 2013). Mapping its occurrence in other canyons is an important next step in connecting boundary mixing and 507 deep-ocean upwelling on a global scale. 508

APPENDIX

Analytical solution of standing wave patterns in the two-slope model

To derive the standing wave modes in the two-slope model, we start with 2D wave equation expressed in terms of the streamfunction ψ in equation.

$$\hat{\psi}_{xx} - c^2 \hat{\psi}_{zz} = 0,\tag{A1}$$

where c is a constant. The general solution for (A1) can be written as:

$$\psi = f(\xi) + g(\eta) \tag{A2}$$

514 where

510

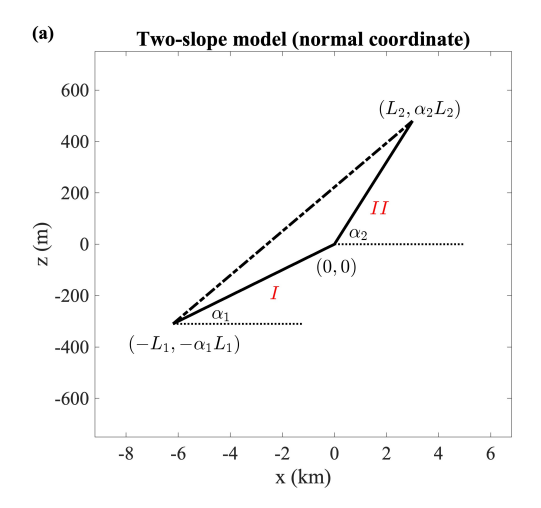
$$\xi = \frac{z}{c} + x,$$

$$\eta = \frac{z}{c} - x$$
(A3)

are coordinates aligned with the wave characteristics. The functions f and g represent arbitrary functions that must satisfy the boundary conditions at I and II, specifically:

$$f(\xi) + g(\eta) = 0$$
 at boundaries *I* and *II*. (A4)

Since the only constraint in this problem is the boundary condition, it becomes a geometric problem determined by the shape of the domain.



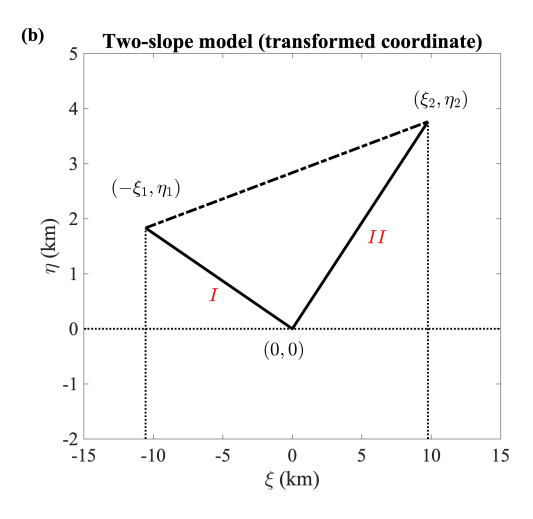


Fig. A1. (a) Two-slope model in the original coordinate system, with dimensions based on the BLT Canyon.

(b) Two-slope model transformed under the coordinate system defined in (A3).).

Solutions to the problem are best expressed by transforming the geometry from the original x-z coordinate system to the $\xi-\eta$ coordinate system, defined in (A3). The three corners in Fig. A1a, namely $(-L_1, -\alpha_1 L_1)$, (0,0), and $(L_2, \alpha_2 L_2)$, are then transformed into the new coordinates $(-\xi_1, \eta_1)$, (0,0), and (ξ_2, η_2) in Fig. A1b, with

$$\xi_1 = \left(\frac{\alpha_1 + c}{c}\right) L_1, \quad \eta_1 = \left(\frac{c - \alpha_1}{c}\right) L_1,$$

$$\xi_2 = \left(\frac{\alpha_2 + c}{c}\right) L_2, \quad \eta_2 = \left(\frac{\alpha_2 - c}{c}\right) L_2.$$
(A5)

We define $f(\xi) = F(\xi)$ for $\xi \in [0, \xi_2]$. At boundary II, characterized by the line function $\eta = \frac{\eta_2}{\xi_2} \xi$, the boundary condition (A4) must be satisfied, leading to:

$$g(\eta) = -f(\xi)\Big|_{II} = -F(\xi)\Big|_{II} = -F\left(\frac{\xi_2}{\eta_2}\eta\right), \text{ for } \eta \in [0, \eta_2].$$
 (A6)

Similarly, boundary I is represented by the line $\eta = -\frac{\eta_1}{\xi_1} \xi$. Applying the boundary condition (A4) results in:

$$f(\xi) = -g(\eta)\Big|_{I} = F\left(\frac{\xi_{2}}{\eta_{2}}\eta\right)\Big|_{I} = F\left(-\frac{\xi_{2}}{\eta_{2}}\frac{\eta_{1}}{\xi_{1}}\xi\right), \quad \text{for } \xi \in [-\xi_{1}, 0].$$
 (A7)

Thus, the full solution for $\hat{\psi}$ can be written as:

$$\hat{\psi}(\xi,\eta) = f(\xi) + g(\eta),\tag{A8}$$

530 where

$$f(\xi) = \begin{cases} F(\xi), & \text{if } \xi \in [0, \xi_2], \\ F\left(-\frac{\xi_2}{\eta_2} \frac{\eta_1}{\xi_1} \xi\right), & \text{if } \xi \in [-\xi_1, 0], \end{cases}$$

$$g(\eta) = -F\left(\frac{\xi_2}{\eta_2} \eta\right).$$
(A9)

Now we determine the boundary conditions that the 1D function F must satisfy. The first derivative of ψ , which represents the velocity field, has to be well-defined at $\xi = 0$. This leads to the condition:

$$f'(\xi \to 0^{-}) = f'(\xi \to 0^{+}),$$

$$-\frac{\xi_{2}}{\eta_{2}} \frac{\eta_{1}}{\xi_{1}} F'(\xi = 0) = F'(\xi = 0),$$

$$F'(\xi = 0) = 0.$$
(A10)

Additionally, a gauge transformation of the form $f \to f + C$ and $g \to g - C$, where C is any constant, does not change $\psi = f + g$. Therefore, without loss of generality, we adopt the convention $F(\xi = \xi_2) = 0$.

With the boundary conditions:

$$F'(\xi = 0) = 0, \quad F(\xi = \xi_2) = 0,$$
 (A11)

the normal modes satisfying these conditions can be expressed as:

$$F_n(\xi) = \cos\left(\frac{(2n-1)\pi\xi}{2\xi_2}\right). \tag{A12}$$

Thus, the streamfunction for mode n can be written as:

$$\hat{\psi}_n(\xi,\eta) = \begin{cases} F_n(\xi) - F_n\left(\frac{\xi_2}{\eta_2}\eta\right), & \text{if } \xi \in [0,\xi_2], \\ F_n\left(-\frac{\xi_2}{\eta_2}\frac{\eta_1}{\xi_1}\xi\right) - F_n\left(\frac{\xi_2}{\eta_2}\eta\right), & \text{if } \xi \in [-\xi_1,0]. \end{cases}$$
(A13)

From the streamfunction expressions for each mode, one can derive the corresponding wave modes for $\hat{u} = \hat{\psi}_z$, $\hat{w} = -\hat{\psi}_x$, and $\hat{p} = -i\omega \int \hat{u} \, dx$. The explicit forms of these fields are omitted here for brevity.

- Acknowledgments. The BLT program is supported by the U.S. National Science Foundation (grant OCE-1756264) and the U.K. Natural Environment Research Council (grant NE/S001433/1). The 543 simulations presented here were supported by computational resources provided by the National 544 Center for Atmospheric Research (NCAR), sponsored by the National Science Foundation, using the Derecho supercomputer (doi:10.5065/5dfh-8a30). The authors are grateful to the BLT team, 546 especially Bethan Wynne-Cattanach, Nicole Couto, Henri Drake, Arnaud Le Boyer, Herle Mercier, 547 Marie-Jose Messias, Xiaozhou Ruan, Carl Spingys, Bieito Fernandez Castro, Hans van Haren, for their efforts in carrying out the BLT experiment and collecting the data. We also thank Xiaozhou 549 Ruan and Jean-Michel Campin for their help with the simulations, and Yidongfang Si, Carl Wunsch, 550 Glenn Fierl, Bethan Wynne-Cattanach, Henri Drake, Wanying Kang, and Shuang Wang for valuable discussions. 552
- Data availability statement. The mooring datasets from the BLT programme used in this study are publicly available through DRYAD at doi:10.5061/dryad.v15dv424f (Voet et al. (2024)). Simulation outputs and analysis scripts used in this work are available from the corresponding author upon reasonable request.

557 References

- Alberty, M., S. Billheimer, M. Hamann, C. Ou, V. Tamsitt, A. Lucas, and M. Alford, 2017: A reflecting, steepening, and breaking internal tide in a submarine canyon. *Journal of Geophysical Research: Oceans*, **122** (**8**), 6872–6882.
- Alford, M. H., and P. MacCready, 2014: Flow and mixing in juan de fuca canyon, washington. *Geophysical Research Letters*, **41** (**5**), 1608–1615.
- Alford, M. H., and R. Pinkel, 2000: Observations of overturning in the thermocline: The context of ocean mixing. *Journal of Physical Oceanography*, **30** (**5**), 805–832.
- Alford, M. H., and Coauthors, 2025: Buoyancy flux and mixing efficiency from direct, near-bottom turbulence measurements in a submarine canyon. *Journal of Physical Oceanography*, **55** (2), 97–118.
- Aslam, T., R. A. Hall, and S. R. Dye, 2018: Internal tides in a dendritic submarine canyon. *Progress*in Oceanography, **169**, 20–32.

- Bellerjeau, C., M. H. Alford, A. Le Boyer, G. Dematteis, A. Naveira Garabato, G. Voet, N. Couto,
- and B. L. Wynne-Cattanach, 2025: Pathways to turbulent dissipation in a submarine canyon.
- Geophysical Research Letters, **52** (**7**), e2024GL113 526.
- Cacchione, D. A., L. F. Pratson, and A. Ogston, 2002: The shaping of continental slopes by internal tides. *Science*, **296** (**5568**), 724–727.
- Callies, J., and R. Ferrari, 2018: Dynamics of an abyssal circulation driven by bottom-intensified mixing on slopes. *Journal of physical oceanography*, **48** (**6**), 1257–1282.
- ⁵⁷⁷ Carter, G., 2010: Barotropic and baroclinic m 2 tides in the monterey bay region. *Journal of*⁵⁷⁸ *Physical Oceanography*, **40 (8)**, 1766–1783.
- Chen, X., and S. E. Allen, 1996: The influence of canyons on shelf currents: A theoretical study.

 Journal of Geophysical Research: Oceans, 101 (C8), 18 043–18 059.
- De Lavergne, C., G. Madec, J. Le Sommer, A. G. Nurser, and A. C. N. Garabato, 2016: On the consumption of antarctic bottom water in the abyssal ocean. *Journal of Physical Oceanography*, 46 (2), 635–661.
- Drake, H. F., R. Ferrari, and J. Callies, 2020: Abyssal circulation driven by near-boundary mixing:
 Water mass transformations and interior stratification. *Journal of Physical Oceanography*, **50** (8),
 2203–2226.
- Egbert, G. D., and S. Y. Erofeeva, 2002: Efficient inverse modeling of barotropic ocean tides.

 Journal of Atmospheric and Oceanic Technology, 19 (2), 183–204, https://doi.org/10.1175/
 1520-0426(2002)019(0183:EIMOBO)2.0.CO;2.
- Ferrari, R., A. Mashayek, T. J. McDougall, M. Nikurashin, and J.-M. Campin, 2016: Turning ocean mixing upside down. *Journal of Physical Oceanography*, **46** (7), 2239–2261.
- Gaspar, P., Y. Grégoris, and J.-M. Lefevre, 1990: A simple eddy kinetic energy model for simulations of the oceanic vertical mixing: Tests at station papa and long-term upper ocean study site. *Journal of Geophysical Research: Oceans*, **95** (**C9**), 16 179–16 193.
- Gordon, R., and N. Marshall, 1976: Submarine canyons: Internal wave traps? *Geophysical Research Letters*, **3 (10)**, 622–624.

- ⁵⁹⁷ Grimshaw, R., P. Baines, and R. Bell, 1985: The reflection and diffraction of internal waves from
- the junction of a slit and a half-space, with application to submarine canyons. *Dynamics of*
- *atmospheres and oceans*, **9 (2)**, 85–120.
- Hall, R. A., T. Aslam, and V. A. Huvenne, 2017: Partly standing internal tides in a dendritic
- submarine canyon observed by an ocean glider. Deep Sea Research Part I: Oceanographic
- 802 *Research Papers*, **126**, 73–84.
- Hall, R. A., and G. S. Carter, 2011: Internal tides in monterey submarine canyon. Journal of
- Physical Oceanography, **41** (1), 186–204.
- Hamann, M. M., M. H. Alford, A. J. Lucas, A. F. Waterhouse, and G. Voet, 2021: Turbulence
- driven by reflected internal tides in a supercritical submarine canyon. Journal of Physical
- oceanography, **51** (2), 591–609.
- Hotchkiss, F. S., and C. Wunsch, 1982: Internal waves in hudson canyon with possible geological
- implications. Deep Sea Research Part A. Oceanographic Research Papers, 29 (4), 415–442.
- Huvenne, V., and B. Thornton, 2020: Cruise report no. 66 rrs discovery cruise dy 108-109. *National*
- Oceanography Centre, Southampton, Report.
- Kang, D., and O. Fringer, 2012: Energetics of barotropic and baroclinic tides in the monterey bay
- area. Journal of Physical Oceanography, **42** (2), 272–290.
- Key, S. A., 1999: Internal tidal bores in the monterey canyon. Ph.D. thesis, Monterey, California.
- Naval Postgraduate School.
- Kunze, E., L. K. Rosenfeld, G. S. Carter, and M. C. Gregg, 2002: Internal waves in monterey
- submarine canyon. *Journal of physical oceanography*, **32 (6)**, 1890–1913.
- Le Souëf, K. E., and S. Allen, 2014: Physical modeling of tidal resonance in a submarine canyon.
- Journal of Geophysical Research: Oceans, 119 (2), 1324–1343.
- Leaman, K. D., and T. B. Sanford, 1975: Vertical energy propagation of inertial waves: A vector
- spectral analysis of velocity profiles. *Journal of Geophysical Research*, **80** (**15**), 1975–1978.
- Lellouche, J.-M., and Coauthors, 2021: The copernicus global 1/12° oceanic and sea ice glorys12
- reanalysis. Frontiers in Earth Science, **9**, 698 876, https://doi.org/10.3389/feart.2021.698876.

- Levine, M. D., and T. J. Boyd, 2006: Tidally forced internal waves and overturns observed on a slope: Results from home. *Journal of physical oceanography*, **36** (6), 1184–1201.
- Lorke, A., F. Peeters, and A. Wüest, 2005: Shear-induced convective mixing in bottom boundary layers on slopes. *Limnology and Oceanography*, **50** (**5**), 1612–1619.
- Ma, Y., R. Ferrari, and K. Polzin, 2025: A simple model for tidally forced standing waves in a submarine canyon. *Journal of Physical Oceanography*.
- Marshall, J., A. Adcroft, C. Hill, L. Perelman, and C. Heisey, 1997: A finite-volume, incompressible navier stokes model for studies of the ocean on parallel computers. *Journal of Geophysical Research: Oceans*, **102** (**C3**), 5753–5766.
- Martini, K., M. Alford, J. Nash, E. Kunze, and M. Merrifield, 2007: Diagnosing a partly standing internal wave in mamala bay, oahu. *Geophysical Research Letters*, **34** (**17**).
- Masunaga, E., M. H. Alford, A. J. Lucas, and A. R.-M. Freudmann, 2023: Numerical simulations
 of internal tide dynamics in a steep submarine canyon. *Journal of Physical Oceanography*,
 53 (11), 2669–2686.
- Munk, W., and C. Wunsch, 1998: Abyssal recipes ii: energetics of tidal and wind mixing. *Deep*Sea Research Part I: Oceanographic Research Papers, **45** (**12**), 1977–2010, https://doi.org/

 https://doi.org/10.1016/S0967-0637(98)00070-3.
- Munk, W. H., 1966: Abyssal recipes. *Deep sea research and oceanographic abstracts*, Elsevier, Vol. 13, 707–730.
- Naveira Garabato, A. C., and Coauthors, 2025: Connecting mixing to upwelling along the ocean's sloping boundary. https://doi.org/10.22541/essoar.175767179.90159335/v1.
- Petruncio, E. T., L. K. Rosenfeld, and J. D. Paduan, 1998: Observations of the internal tide in monterey canyon. *Journal of Physical Oceanography*, **28** (**10**), 1873–1903.
- Polzin, K., 1996: Statistics of the richardson number: Mixing models and finestructure. *Journal*of physical oceanography, **26** (**8**), 1409–1425.
- Polzin, K. L., and T. J. McDougall, 2022: Mixing at the ocean's bottom boundary. *Ocean mixing*, Elsevier, 145–180.

- Pratt, L. L., and J. A. Whitehead, 2007: Rotating hydraulics: nonlinear topographic effects in the ocean and atmosphere, Vol. 36. Springer Science & Business Media. 652
- Rosenfeld, L. K., J. D. Paduan, E. T. Petruncio, and J. E. Goncalves, 1999: Numerical simulations 653 and observations of the internal tide in a submarine canyon. Proceedings of the 11th'Aha Huliko'a Hawaiian Winter Workshop, 63–71. 655
- Ruan, X., and R. Ferrari, 2021: Diagnosing diapycnal mixing from passive tracers. Journal of 656 *Physical Oceanography*, **51** (3), 757–767. 657
- Si, Y., R. Ferrari, and G. Voet, 2025: Tidally induced turbulence in the abyssal ocean. arXiv preprint arXiv:2509.05869. 659
- Swart, N., S. E. Allen, and B. Greenan, 2011: Resonant amplification of subinertial tides in a 660 submarine canyon. Journal of Geophysical Research: Oceans, 116 (C9). 661
- Taylor, G. I., 1922: Tidal oscillations in gulfs and rectangular basins. *Proceedings of the London Mathematical society*, **2** (**1**), 148–181. 663
- Tsujino, H., and Coauthors, 2018: Jra-55 based surface dataset for driving ocean–sea-ice models 664 (jra55-do). Ocean Modelling, **130**, 79–139, https://doi.org/10.1016/j.ocemod.2018.07.002. 665
- Umlauf, L., and H. Burchard, 2011: Diapycnal transport and mixing efficiency in stratified boundary layers near sloping topography. Journal of physical oceanography, 41 (2), 329–345. 667
- Van Haren, H., G. Voet, M. H. Alford, B. Fernández-Castro, A. C. N. Garabato, B. L. Wynne-668 Cattanach, H. Mercier, and M.-J. Messias, 2024: Near-slope turbulence in a rockall canyon. Deep Sea Research Part I: Oceanographic Research Papers, **206**, 104 277. 670
- Voet, G., M. Alford, K. Polzin, A. Naveira Garabato, S. Kawamato, and H. Dufel, 2024: 671 Boundary layer turbulence and abyssal recipes (blt): moored observations. Dryad https://doi.
- org/10.5061/dryad. v15dv424f. 673

672

Wain, D., M. Gregg, M. Alford, R.-C. Lien, R. Hall, and G. Carter, 2013: Propagation and 674 dissipation of the internal tide in upper monterey canyon. Journal of geophysical research: 675 Oceans, 118 (10), 4855–4877.

- Waterhouse, A. F., J. A. Mackinnon, R. C. Musgrave, S. M. Kelly, A. Pickering, and J. Nash, 2017:
- Internal tide convergence and mixing in a submarine canyon. Journal of Physical Oceanography,
- **47 (2)**, 303–322.
- Weatherall, P., and Coauthors, 2023: The gebco 2023 grid. NERC EDS British Oceanographic
- Data Centre, NOC, URL https://doi.org/10.5285/f98b053b-0cbc-6c23-e053-6c86abc0af7b.
- Webb, A., and S. Pond, 1986: A modal decomposition of the internal tide in a deep, strongly
- stratified inlet: Knight inlet, british columbia. Journal of Geophysical Research: Oceans,
- **91 (C8)**, 9721–9738.
- Winters, K. B., 2015: Tidally driven mixing and dissipation in the stratified boundary layer above
- steep submarine topography. *Geophysical Research Letters*, **42** (**17**), 7123–7130.
- Wynne-Cattanach, B. L., M. H. Alford, and coauthors, 2025: Boundary-interior exchange quanti-
- fied with a long-term moored volume budget. *Journal of Physical Oceanography*.
- 689 Wynne-Cattanach, B. L., and Coauthors, 2024: Observations of diapycnal upwelling within a
- sloping submarine canyon. *Nature*, **630** (**8018**), 884–890.
- Zhang, W. G., T. F. Duda, and I. A. Udovydchenkov, 2014: Modeling and analysis of internal-tide
- generation and beamlike onshore propagation in the vicinity of shelfbreak canyons. *Journal of*
- ⁶⁹³ *physical oceanography*, **44** (3), 834–849.
- ⁶⁹⁴ Zhao, Z., M. H. Alford, R.-C. Lien, M. C. Gregg, and G. S. Carter, 2012: Internal tides and mixing
- in a submarine canyon with time-varying stratification. Journal of Physical Oceanography,
- **42 (12)**, 2121–2142.